

## FEDSM-ICNMM2010-30255

### TRANSIENT NUMERICAL COMPUTATION OF THE TEMPERATURE OF ELECTRONIC DEVICES IN PASSENGER CARS: FLOW SIMULATION IN ELECTRONICS CAVITIES

**Dr. Florence MICHEL**  
Daimler AG  
Sindelfingen, Germany

**Prof. Bernard DESMET**  
Laboratoire de Mécanique et Energétique  
Valenciennes, France

#### ABSTRACT

To compute the temperature of an electronic system submitted to time-dependent thermal loads, the problem of multi-scale coupled heat transfer modes is solved by means of co-simulation strategies. These coupling strategies use adapted codes for the prediction of each transfer mode, e.g. a CFD code for the computation of convection and a FE code for conduction. In this paper, numerical models to solve the flow in typical electronic enclosures are investigated, in particular regarding mesh requirements and turbulence modeling. First, the accuracy of a steady-state approach for the computation of natural convection in a cavity heated from below is examined for a large range of Rayleigh number covering time-dependent convection. Then, a steady-state method for fan flow simulation is presented and validated in comparison with the fan performance curve measured in a test-rig. Finally, different numerical models for flow computation through thin grills of an electronic system are discussed regarding the fan mass flow rate and the establishing pressure distribution.

#### INTRODUCTION

For multiple reasons such as user accessibility and assembly facilities for serial production, electronic devices are often located in small cavities of the vehicle, where they are susceptible of overheating. In order to ensure a reliable operation of an electronic device, its thermal behavior is evaluated in a digital prototype. Of particular interest is to predict the time period, during which the electronic system works within its optimal operating temperature range. In a companion paper [1], coupling codes strategies are proposed to predict the temperature of an electronic system in its environment in the vehicle under time-dependent operating conditions and thermal loads. The conduction and convection heat transfer modes are computed with adapted codes, e.g. a CFD

code for convection and a FE code for conduction. The FE code runs transient and performs the energy balance for each time-step, while the convection heat rate is calculated by the CFD code separately. Due to the very high numerical effort of this coupling method, a steady-state approach is used to solve the conservation equations of the flow. By applying these co-simulation strategies, it is assumed that one computation of the flow based on prescribed temperature boundary conditions is sufficient to reproduce the correct flow structure and provide reasonable heat flux predictions requested at the fluid-solid interface. The co-simulation strategies are investigated by means of two complex electronic systems: a back battery in a sealed spare-wheel cavity and a sound amplifier assembled in a compartment under the passenger's feet (Fig. 1).



**Figure 1. Back battery in the spare-wheel cavity (left)  
and sound amplifier in the feet compartment (right)**

Use cases are set up to test the thermal response of an electronic system in the car. Standard use cases consist of a first phase of pre-conditioning with warming-up, followed by a period of thermal load, e.g. uphill drive with load trailers, completed by thermal soak with engine shut off. At the end of the pre-conditioning period, the solid temperatures in the cavity have reached a permanent state. Convection approaches the conductivity state with a stratified temperature distribution.

In passive cooled cavities as for the battery, the development of convective rolls depends on the wall temperature distribution and on the geometrical wall configuration [2]. Regarding the battery during the driving and soak phases, the time-dependent environment temperatures yield to different flow states, from oscillating to turbulent regimes according to Rayleigh numbers ranging between  $Ra = 9.7 \times 10^5$  and  $Ra = 4.6 \times 10^7$  (Fig. A.1 and A.2 in annex). In [3], the authors noticed experimentally that several minutes are required for the flow to reach a full developed state in the case of time-dependent convection, while several hours are required in the case of steady convection. It means that, over the testing time, the flow in the cavity of the battery may never reach a fully developed state. For the computation of the time-dependent convection, different turbulence models have been verified in the literature using DNS [4], LES with SGS (subgrid scale) [5] and URANS (unsteady RANS) [6]. Several attempts at steady-state computations with RANS turbulence models [7] showed some limitations, in particular in the prediction of the turbulent heat flux in the whole cavity. In view of this stability problem, it is necessary to verify that the CFD code used for the co-simulation is able to predict correctly the flow structure and the heat flux at the interface by means of steady-state RANS computations.

As for the sound amplifier, most of electronic devices are equipped with internal axial fans, drawing ambient air into the system. The fan induced flow rate is then leaving the device through loose outlets or outlet grills. The pressure drop of the electronic system due to the complex geometry can be expressed generally by:

$$\Delta p_{stat} = c_1 \rho \dot{V} + c_2 \rho \dot{V}^2 \quad (1)$$

The operating point is defined as the fan pressure rise condition, for which the fan and electronic system are in a stable equilibrium. In the case of the sound amplifier submitted to standard use cases, the Reynolds number is found of  $Re = 1.1 \times 10^3$  and the Grashof number of  $Gr = 9.6 \times 10^6$  (Fig. A.3 and A.4 in annex). In this range, the strength of the shear forces of the fan flow inhibits the development of a secondary flow that may develop at a heated module and slows down the enlargement of the internal thermal boundary layer [8, 9]. Therefore, it is necessary to introduce a model for fan flow simulation in the CFD code and verify it. As outlet grills may contribute to a significant part of the total pressure drop of the system, numerical models for outlet grills must be investigated as well. The CFD code used to compute the convection heat transfer mode is presented in the first part.

## NOMENCLATURE

A	[m <sup>2</sup> ]	Surface area
$c_p$	[J kg <sup>-1</sup> K <sup>-1</sup> ]	Specific heat capacity
$D_H$	[m]	Hydraulic diameter

Gr	[-]	Grashof number
H	[m]	Generic length, i.e. height
h	[W m <sup>-2</sup> K <sup>-1</sup> ]	Heat transfer coefficient
k	[-]	Pressure loss coefficient
k	[W m <sup>-1</sup> K <sup>-1</sup> ]	Thermal conductivity
L	[m]	Characteristic length
Nu	[-]	Nusselt number
p	[N m <sup>-2</sup> ]	Pressure
$\dot{q}$	[W m <sup>-2</sup> ]	Heat flux
Ra	[-]	Rayleigh number
Re	[-]	Reynolds number
T	[K]	Temperature
u	[m s <sup>-1</sup> ]	Velocity magnitude
$u_i, u_j$	[m s <sup>-1</sup> ]	Velocity components
$\dot{V}$	[m <sup>3</sup> s <sup>-1</sup> ]	Volume flow rate
$x_i, x_j$	[m]	Cartesian coordinates
y	[m]	Normal distance from the wall to the near-wall cell node
y+	[-]	Dimensionless normal distance from wall
Greek symbols		
$\epsilon$	[-]	Emissivity (radiation)
$\mu$	[kg m <sup>-1</sup> s <sup>-1</sup> ]	Dynamic (molecular) viscosity
$\nu$	[m <sup>2</sup> s <sup>-1</sup> ]	Kinematic viscosity
$\rho$	[kg m <sup>-3</sup> ]	Mass density
$\omega$	[min <sup>-1</sup> ]	Angular velocity
Physical constant		
$g = 9.81$	[m s <sup>-2</sup> ]	Gravitational acceleration
Subscripts and superscripts		
c		Cold
conv		Convection
f		Fluid
g		Grill
h		Hot
m		Mean
n1		Node of the near-wall cell
o		Orifice
s		Solid
stat		Static
t		Turbulent

## FLOW SOLVER STAR-CD

The whole study is carried out using the commercial finite volume CFD code STAR-CD [10]. To mesh complex geometries with shaped and curved surfaces, trimmed meshes are used. They are based on hexahedral cells with trimmed type polyhedral near the subsurface. Moreover, for reasonable computing times eddy viscosity models are used to close the system described by the three RANS equations. Any of these models is based on the eddy conductivity concept, for which the turbulent heat flux follows a similar law as the Fourier law for diffusive conduction. It assumes the simple gradient diffusion hypothesis (SGDH).

With  $\sigma_t$  the turbulent Prandtl number:

$$\bar{\rho} c_p \overline{u_j'' T_f''} = -\frac{\mu_t c_p}{\sigma_t} \frac{\partial \overline{T_f}}{\partial x_j} = -k_t \frac{\partial \overline{T_f}}{\partial x_j} \quad (2)$$

In STAR-CD, the evaluation of the convection heat transfer is based on the temperature of the first near-wall cell, as illustrated in Fig. 2.

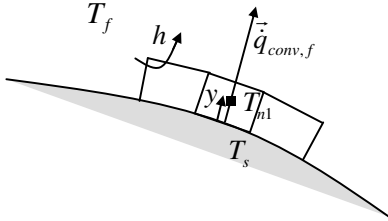


Figure 2. Convection heat flux at the fluid-solid interface.

With  $y$  the normal distance from the wall to the near-wall cell node, the convection heat flux at the interface is approximated by STAR-CD by:

$$\dot{q}_{conv,f} = k \frac{T_s - T_{n1}}{y} \quad (3)$$

The governing equations of mass, momentum and energy conservation are discretized by the finite volume method. The second-order differencing schemes MARS (monotone advection and reconstruction scheme) is used for convection fluxes and turbulent quantities and CD (central differencing) for density. The coupling between velocity and pressure fields is solved by the SIMPLE (semi-implicit method for pressure linked equations) solution algorithm.

## BUOYANCY-DRIVEN FLOW

The investigation is conducted for the well-documented extended Rayleigh-Bénard convection in an enclosure with conducting sidewalls. The study is carried out for a large range of Rayleigh numbers covering steady and time-dependent convection in case of air. Several aspects of the steady-state approach are questioned, in particular the effect of initial conditions on the convection structure and the convergence of the eddy viscosity models for the computation of time-dependent convection. The results are compared with experimental and numerical studies from the literature considering two benchmark cases: a rectangular box [3, 11] and a cubical cavity [5, 12].

### Structure of the flow, rectangular box

The numerical model consists of a fluid cell enclosed in thin glass plates and differentially heated by copper plates maintained at constant temperature (Fig. 3). The vertical temperature distribution is nearly linear at the sidewalls. The results are presented for a horizontal cavity.

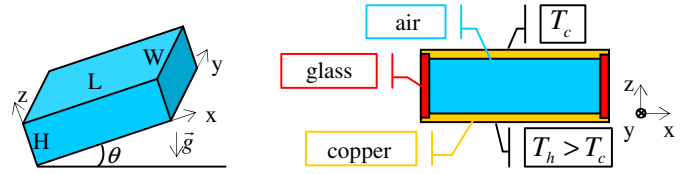


Figure 3. Numerical model of the rectangular cavity; fluid layer (left); (x,z) section (right).

**Initialization** Assuming the flow initially isothermal without motion, steady-state 3D simulations provide longitudinal rolls instead of the transversal ones as described by [3]. Different types of initialization are investigated to reproduce the correct flow structure. First, a 2D computation is carried out in the plane perpendicular to the axis of the expected transversal rolls. The resulting flow and thermal fields are used as initialization for the 3D computation. Two different types of boundary conditions are investigated for the 2D computation (Fig. 4):

- with differential temperature boundary conditions at the top and bottom plates, called differential temperature initialization;
- with a wall movement condition at the top and bottom plates, called moving wall initialization. Velocity vectors  $\vec{u}_x$  of x-component only are assigned at the middle of the expected convection rolls.

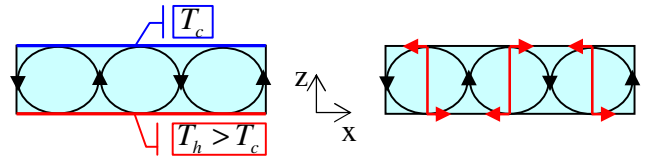


Figure 4. Initialization type for the 2D computation: differential temperature (left); moving wall (right).

**Steady-state convection** The flow is computed in a cavity of 10:4:1 aspect ratio for both initialization types at a Rayleigh number of  $Ra = 4 \times 10^3$ . The differential temperature initialization provides a transversal ten-roll structure, instead of the transversal nine-roll structure described by [3]. With the moving wall initialization, a structure with nine rolls is obtained, as shown in Fig. 5.

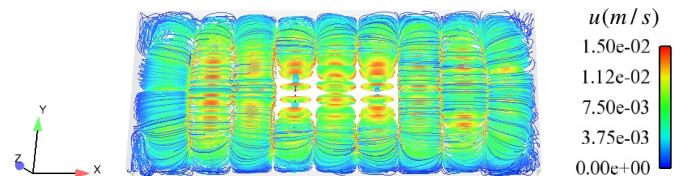


Figure 5. Streamlines at  $Ra = 4 \times 10^3$  in a 10:4:1 cavity with moving wall initialization.

**Time-dependent convection** The flow is computed in a cavity of 4:2:1 aspect ratio for Rayleigh numbers in the range  $[4 \times 10^4; 2.5 \times 10^5]$  using the differential temperature initialization. For  $Ra = 1.5 \times 10^5$  and  $Ra = 2.5 \times 10^5$ , a complex structure is obtained based on two lateral rolls, which is in agreement with the results described in [3]. Moreover, the maximum vertical velocity component in the mid-plane  $z/H = 0.5$  is shown in Fig. 6. It shows a good agreement with the literature over the whole range of Rayleigh numbers.

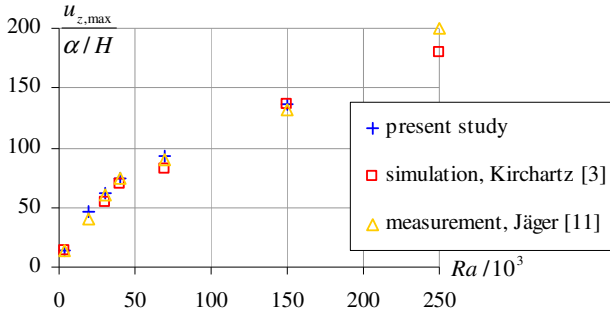


Figure 6. Maximum vertical velocity in the mid-plane  $z/H = 0.5$  of the cavity 4:2:1.

### Heat transfer rate, cubical cavity

The numerical model consists of a cubical fluid cell enclosed in thin glass plates and differentially heated from below, very similar to Fig. 3. Results are presented for a horizontal cavity.

**Initialization** The flow is supposed initially isothermal and at rest. A correct flow structure is reached after transition without requiring to the 2D initialization.

**Turbulence modeling** Different turbulence models are investigated for Rayleigh numbers of  $Ra = 10^6$  and  $Ra = 10^7$ . The mean Nusselt number computed with a fine mesh using  $10^9$  grid nodes is examined, as shown in Fig. 7. The standard low-Re  $k-\epsilon$  model provides the best agreement with the results from the literature, within 3% for  $Ra = 10^6$  and 8% for  $Ra = 10^7$ .

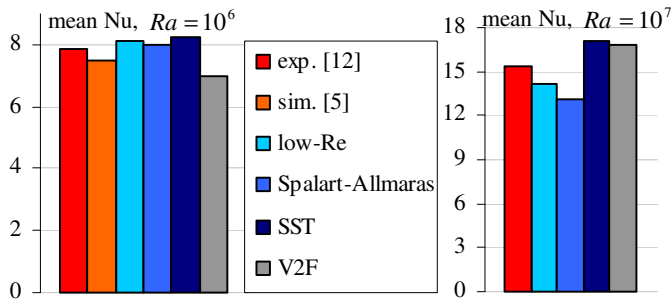


Figure 7. Turbulence modeling study with a  $10^9$  nodes grid: comparison of the mean Nusselt number with literature.

**Flow structure and heat flux distribution** A summary of the structures obtained can be found in Table 1.

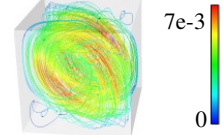
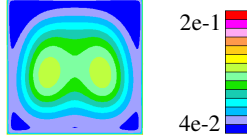
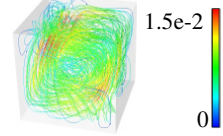
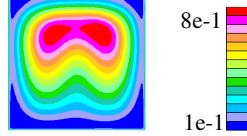
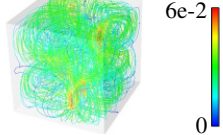
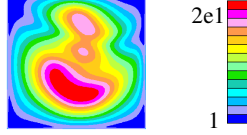
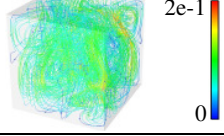
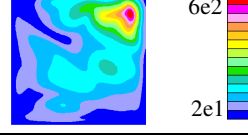
Ra	streamlines $u(m/s)$	heat flux ( $W/m^2$ )
$4 \times 10^4$		
$10^5$		
$10^6$		
$10^7$		

Table 1. Streamlines and heat flux obtained in the present study.

The structures obtained after transition are found in good agreement with [5], except at  $Ra = 10^5$ . Also, the distribution of heat flux on the lower and upper walls is reasonable for steady-state convection. However, the distributions computed in the present study at higher Rayleigh numbers show more irregularities than described in [5]. Moreover, a full convergence of the residuals could not be reached, yielding to a strong variation of the heat flux over the iterations. To improve the convergence of the residuals, an URANS computation has been performed using a time-step of  $10^{-3}$ s with 500 inner iterations over a running time of  $10^{-1}$ s. The resulting mean Courant number is equal to  $4 \times 10^2$ . Again, the averaged wall heat flux shows strong variations over the inner iterations. Therefore, the divergence of heat flux over the iterations does not result from the steady-state approach, but from turbulence modelling. This is examined in the following.

### Mesh independency for heat flux prediction

Different structured and uniform grids using solely hexahedral cells have been generated (Table B.1 in annex). The averaged Nusselt numbers on the lower or upper wall are provided by, respectively:

$$\overline{Nu}|_{z=0} = \frac{H}{k(T_h - T_c)} \bar{q}|_{z=0} \quad (4)$$

$$\overline{Nu}|_{z=H} = -\frac{H}{k(T_h - T_c)} \bar{q}|_{z=H} \quad (5)$$

For an estimation of the averaged Nusselt number independently of the grid, an extrapolation is performed in the Richardson chart. This provides a theoretical value of the averaged Nusselt number for a grid using an infinite number of nodes, as illustrated in Fig. 8.

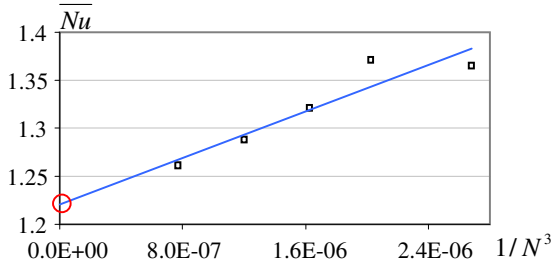


Figure 8. Extrapolation of the averaged Nusselt number on a horizontal wall in the Richardson chart,  $Ra = 10^4$ .

The comparison of the averaged Nusselt number with the results obtained in [5, 12] is shown in Fig. 9. The error resulting from the large variations of heat flux at  $Ra = 10^6$  and  $Ra = 10^7$  is indicated.

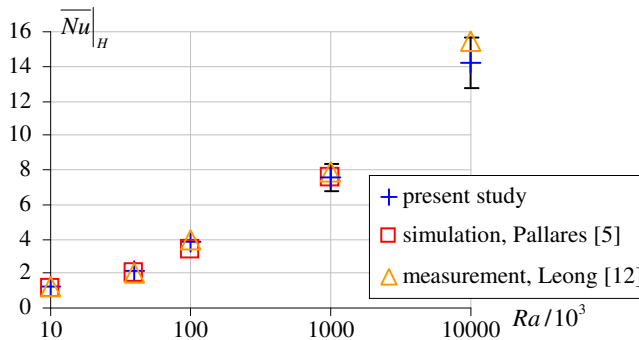


Figure 9. Averaged Nusselt number on the upper wall ( $z=H$ ) in comparison with literature.

A good agreement is found for Rayleigh numbers in the range  $[10^4; 10^5]$ . In particular, the difference between the values of Nusselt number measured by [12] and the present predictions are of 2% for  $Ra = 10^4$ , 8.5% for  $Ra = 4 \times 10^4$  and 3.5% for  $Ra = 10^5$ . For higher Rayleigh numbers, the numerical error in the present computations is too large for a reasonable comparison.

**Limits of the numerical model for turbulent flow**

The mean temperature profile is obtained by juxtaposing the temperature mean values in each horizontal thin layer. It is shown in Fig. 10 at  $Ra = 10^7$ , for which the turbulent flow is fully developed. The results shows that the mean temperature in the bulk is not constant, while the mean temperature gradient is found very small or even zero [13]. This difference is attributed to the simple gradient diffusion hypothesis (SGDH) used in this study. For a better prediction of the vertical distribution of mean temperature and thus of the

turbulent heat flux, the four-equation algebraic heat flux model proposed by Hanjalic [14] is currently being implemented in STAR-CD as an extension of the standard low-Re  $k-\epsilon$  turbulence model.

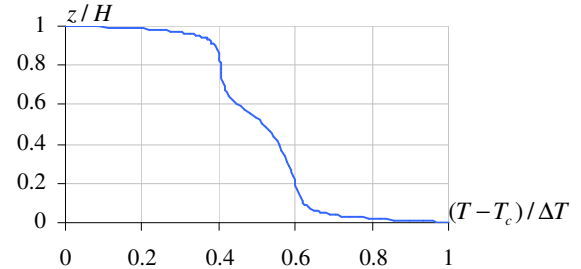


Figure 10. Normalized temperature profile at  $Ra = 10^7$  with the standard low-Re  $k-\epsilon$  turbulence model.

**FORCED CONVECTIVE FLOW**

A steady-state numerical method for fan flow simulation and numerical models for flow computation through thin grills are investigated in the following. The validity of these models is discussed regarding the prediction of the fan mass flow rate and pressure distribution.

**Fan flow computation with MRF**

The fans mounted in the sound-amplifier and TV-tuner are considered for the study (Fig. 11). The operating point of each system has been measured in the fan test-rig at ambient temperature.

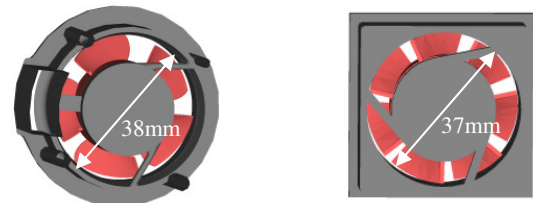
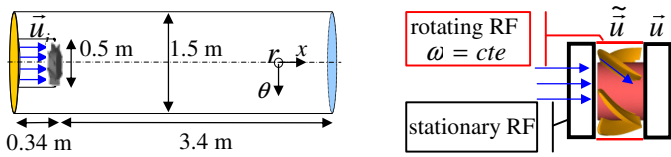


Figure 11. Back view of the fans of the sound amplifier (left) and TV-tuner (right).

**Numerical model**

It is based on the fan test-rig of the supplier (Fig. 12). The fan is positioned perpendicularly at the downstream section of the measurement chamber and subjected to a homogeneous inlet flow. The free outlet chamber is modeled by a cylindrical chamber. A constant axial velocity distribution is imposed at the inlet of the measurement chamber with a given mass flow rate, reproducing the effect of a straightener. A pressure outlet boundary condition is imposed at the far end of the free outlet chamber. The flow is initialized with the ambient pressure and temperature measured in the fan test-rig.



**Figure 12. Numerical model for the computation of the fan flow in the test-rig.**

In the fluid region swept out by the blades, a rotating reference frame is defined. Upstream and downstream, a stationary inertial reference frame is used. With  $\vec{r}$  referring to the position vector relative to the axis of rotation, the relative velocity  $\tilde{\vec{u}}$  in the rotating frame is the difference between the absolute velocity  $\vec{u}$  in the static reference frame and the rotational relative velocity:

$$\tilde{\vec{u}} = \vec{u} - \vec{\omega} \times \vec{r} \quad (6)$$

At the interface between the rotating and the stationary reference frames, the velocities on the stationary side are transformed implicitly into the rotating frame of reference and conversely. Moreover, the spin of the region solved by the rotating reference frame is assigned to the angular fan velocity. The wall boundary of the rotor, which absolute velocity is the angular fan velocity, has a spin number of zero. The wall boundary of the stator attached to the rotating cells, which is not rotating in the stationary frame, is assigned of the opposite spin.

**Turbulence modeling and mesh refinement study** The operating point of the fan installed in the sound amplifier is found in the test-rig for a volume flow rate of  $2.71 \times 10^{-3} \text{ m}^3/\text{s}$ , corresponding to a fan pressure rise of 14.2 Pa. A relatively fine trimmed mesh (T2) generated with STAR-CD with two million cells in the fan region is used (Table B.2 in annex). The fan volume flow rate is found within 0.5% in comparison with the experimental results independently of the turbulence model. Moreover, the Spalart-Allmaras and SST  $k-\omega$  models provide the best agreement for the fan pressure rise within 6%, while a larger discrepancy of 14% is found with the RNG  $k-\epsilon$  model and standard high-Re  $k-\epsilon$  turbulence model using the two-layer approach (Fig. 13).

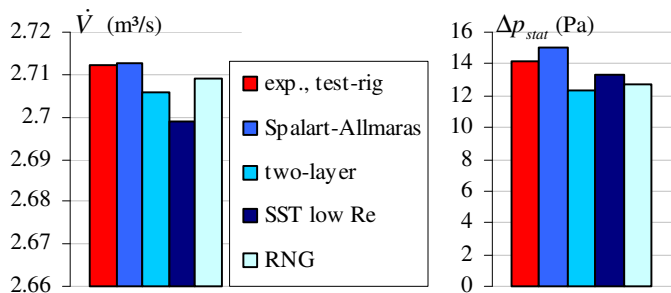


**Figure 13. Turbulence model study using the grid T2; fan flow rate (left) and pressure rise (right) at the operating point.**

Used in electronic systems presenting a complex geometry, the Spalart-Allmaras and SST  $k-\omega$  models diverge rapidly. The two-layer approach is selected as turbulence model for the computation of forced convection in electronic systems. To improve the prediction of the two-layer approach, a mesh refinement study is performed for the fan of the sound amplifier. Several grids using polyhedral cells for a better matching with the curvilinear geometry were generated with STAR-CCM+. For comparable results, only the fan region has been refined (Table B.2). A good agreement with the experimental results is achieved using a grid with minimum six cell layers in the near-wall region (Fig. 14). The difference between experimental and numerical results is equal to 9.5% with the grid using six cell layers in the near-wall region and to 9% with the grid using nine cell layers in the near-wall region.

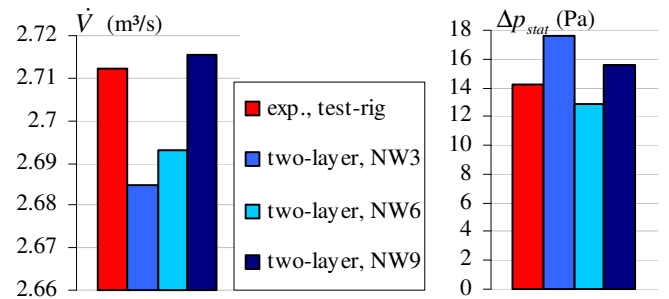


**Figure 14. Mesh refinement study using the two-layer approach; fan flow rate (left) and pressure rise (right) at the operating point.**

The validity of the MRF method is also examined for the fan of the TV-tuner. The operating point with a volume flow rate of  $1.20 \times 10^{-3} \text{ m}^3/\text{s}$  is chosen for the validation, corresponding to a fan pressure rise of 8.87 Pa. A comparable mesh is generated using 6 cell layers in the fan near-wall region and composed of  $1.31 \times 10^6$  cells in the fan region and  $1.38 \times 10^6$  cells elsewhere. According to the previous discussion, the standard high-Re  $k-\epsilon$  turbulence model with the two-layer approach is used in the computation. The volume flow rate and the fan pressure rise are found respectively within 0.5% and 6% in comparison with the experimental results.

### Thin electronic grills

Numerical models for flow simulation through outlet grills are investigated in a TV-tuner. Two populated PCBs are superimposed mounted with different ICs (integrated circuits). The fan investigated in the last paragraph is mounted on the casing, drawing the ambient air into the system. The Reynolds number based on the mean volume flow rate prescribed by the fan is found in the range [6000; 8300]. For flow outlet, the casing is constituted of four grill areas of different vent geometries, as shown in Fig. 15. The geometric parameters of the different outlet grills are provided in annex, Table B.3.

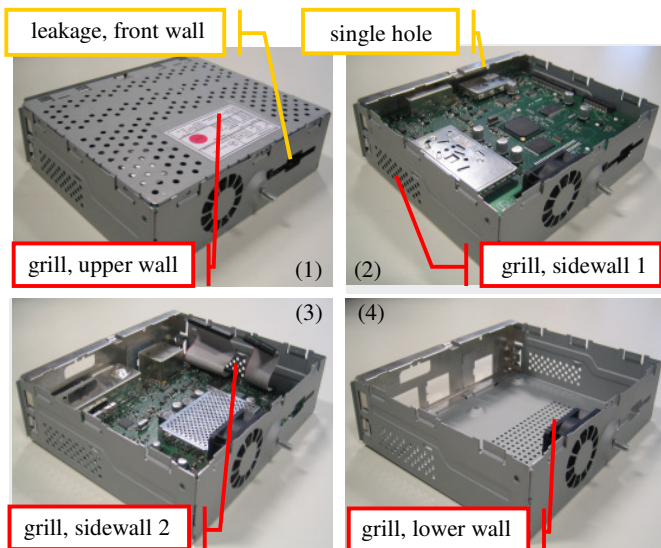


Figure 15. TV-tuner: upper wall (1), upper PCB (2), lower PCB (3), lower wall (4).

Different numerical models for the outlet grills are generated:

- a detailed model of the TV-tuner grills, in which each orifice is solved with several grid cells;
- a model using 2D resistance elements (porous baffle) for the outlet grills;
- and a model using 3D resistance elements (porous region) for the outlet grills.

In a first step, a detailed model of a perforated plate in a test-rig is investigated. A mesh refinement study is carried out for validation. In a second step, a detailed model of the TV-tuner is set up based on the mesh parameters of the perforated plate. The results provided by the porous models are compared with the detailed computation. Due to the complexity of the geometry, the study is performed with STAR-CCM+.

### Perforated plate in a test-rig

The pressure drop and discharge coefficients of a perforated plate have been investigated for a plate installed perpendicularly in a duct and submitted to a homogeneous inlet flow [15, 16]. For small plate thickness to orifice diameter ratio, the pressure drop contribution due to friction losses in the orifice can be neglected.

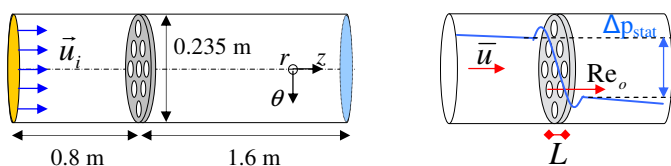


Figure 16. Numerical model for the computation of the perforated plate in the test-rig.

Considering the sole contributions due to the flow constriction and section enlargement upstream and downstream the orifice, the pressure drop through the perforated plate has only an inertial loss contribution (Fig. 16). The static pressure drop of the perforated plate can be expressed as a function of the inflow mean velocity:

$$\Delta p_{stat} = k \frac{\rho u_o^2}{2} = k \left( \frac{A_g}{A_o} \right)^2 \frac{\rho \bar{u}^2}{2} \quad (7)$$

Mühle [16] provides a correlation between the pressure loss coefficient and the geometrical parameters of the perforated plate:

$$k = 1.75 \left( 1 - \frac{A_o}{A_g} \right) + \frac{64}{\text{Re}_o} \frac{L}{d_o} \quad (8)$$

The Reynolds number  $\text{Re}_o$  is based on the mean orifice velocity and diameter. This correlation and measurements carried out in a wind tunnel [17] are used in the following for the model validation.

### Numerical model

A perforated plate of similar free area ratio as in the TV-tuner is chosen for the computation (Table B.4 in annex). The model is based on the test-rig of the wind tunnel. The perforated plate is positioned perpendicularly in the duct and submitted to a homogeneous inlet flow, as illustrated in Fig. 16. A pressure outlet boundary condition is imposed at the far end of the measurement section. The flow is initialized with the ambient pressure and temperature measured in the test-rig.

### Mesh refinement study

The inlet velocity is set constant to  $u_i = 1 \text{ m/s}$ . Three different grids have been generated (Table B.5 in annex). For comparable results, only the region of the perforated plate has been refined. The static pressure drop is evaluated as the difference between the ambient pressure and the static pressure in a parallel section plane located at  $1 \times 10^{-1} \text{ m}$  upstream of the plate. The results of the refinement study can be seen in Fig. 17. The numerical results obtained using the finest mesh (NW5) show a good agreement with the correlation 8 within 8%.

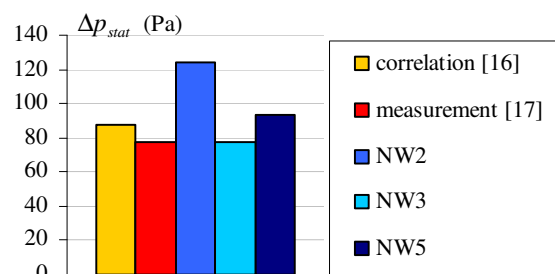


Figure 17. Mesh refinement study: static pressure drop of the perforated plate in the test-rig with an inlet velocity  $u_i = 1 \text{ m/s}$ .

**Pressure loss coefficient** Computations in the test-rig are carried out for inlet velocities of  $u_i = 0.25$  m/s and  $u_i = 0.5$  m/s, according to the range of Reynolds number in the TV-tuner. Moreover, to obtain a general trend of the pressure loss coefficient, an additional computation is performed with an inlet velocity of  $u_i = 3$  m/s. The pressure loss coefficient over the Reynolds number based on the inlet velocity is shown in Fig. 18.

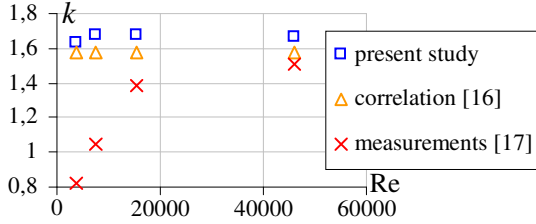


Figure 18. Variation of the pressure loss coefficient of the perforated plate in the test-rig with the Reynolds number.

The pressure loss coefficients predicted by correlation 8 and the present computations are about constant over the range of Reynolds numbers considered, which confirms the main contribution of inertial losses. The strong decrease predicted by the experiments is attributed to a problem of measurement repeatability. The plate pressure loss coefficient is in very good agreement with correlation 8 within 6%. Therefore, the mesh parameters employed can be used in the following study to solve the outlet grills of the TV-tuner.

### Outlet grills of the TV-tuner

Using a porous region, the pressure drop through the perforated plate is calculated based on the Forchheimer's law. With  $L$  the thickness of the perforated plate, the relationship between the plate pressure drop and superficial velocity  $u_i$  in direction  $i$  is given by:

$$\Delta p_{stat} = -L(I_{ij}|\bar{u}_k| + V_{ij})\bar{u}_i \quad (9)$$

$I_{ij}$  and  $V_{ij}$  are diagonal tensors representing respectively the inertial and viscous contributions to pressure losses. Due to its small thickness, the outlet grill can be also modeled as a 2D planar resistance, called porous baffle. It is consequently assumed that the direction of the flow is unchanged as it passes through the baffle. With  $u_n$  the superficial velocity normal to the baffle surface, the plate pressure drop is provided by:

$$\Delta p_{stat} = -\rho(\alpha|\bar{u}_n| + \beta)\bar{u}_n \quad (10)$$

$\alpha$  and  $\beta$ , in analogy with  $I_{ij}$  and  $V_{ij}$ , describe the form drag and permeability of the membrane respectively.

### Numerical models

The geometric surface of the TV-tuner, including the lower and upper populated PCBs, is extracted for mesh generation using polyhedral cells. Only the largest ICs, which may alter the boundary layer growth developing downstream the fan, are taken into account in the model. The mesh of the detailed model is composed of a total of  $1.07 \times 10^7$  cells. The grid of the 2D and 3D porous resistance models is composed of a total of  $8.25 \times 10^6$  cells, i.e.  $2.45 \times 10^6$  less cells than in the detailed model. The numerical models can be seen in Fig. 19.

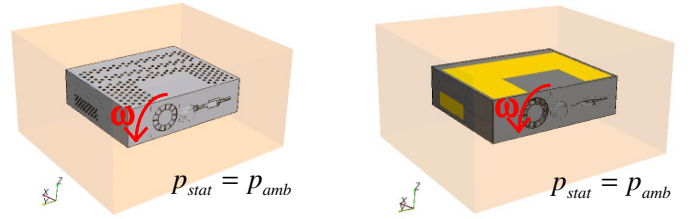


Figure 19. Numerical models for the computation of the grill flow with a detailed model (left) or using porous elements (right).

The fan angular velocity is given as boundary condition to the rotating region. The walls of the environment box are assigned of a constant pressure outlet boundary condition. The flow is considered initially at rest and at ambient pressure.

**Determination of the porous coefficients** First, the range of order of the porosity coefficients is calculated for each grill of the TV-tuner solved in the detailed model. Considering the grill as a planar porous resistance of thickness  $L$ , the grill static pressure drop can be expressed with the grill mass flux  $\dot{M}$  as the sum of an inertial term  $I$  and a viscous term  $V$ :

$$\Delta p_{stat} = I \frac{\dot{M}^2}{\rho} + V\dot{M} \quad (11)$$

Inside the TV-tuner, the static pressure distribution in section planes parallel with the grills is strongly affected by the geometry of the ICs. In order to evaluate the static pressure drop of the outlet grills, section planes are set parallel to the outlet grill up to recovery upstream the grill. The range of order of the inertial and viscous terms is shown in Table 2.

	Inertial term $I$ (-)	Viscous term $V$ (m/s)
Grill, upper wall	$1.94 \times 10^2$	$3.46 \times 10^{-1}$
Grill, lower wall	$4.80 \times 10^1$	$7.34 \times 10^{-1}$
Grill, sidewall 1	$1.95 \times 10^1$	$5.87 \times 10^{-1}$
Grill, sidewall 2	$2.49 \times 10^1$	$5.35 \times 10^{-1}$

Table 2. Estimation of the inertial and viscous contributions to grill pressure losses in the TV-tuner.



The viscous contributions to pressure losses of thin grills can be neglected in comparison with the inertial contribution. Therefore, the grill pressure drop can be expressed as in equation 7. With this assumption, the inertial coefficients for 2D model and tensor for 3D model are respectively provided by:

$$\alpha = \frac{k}{2} \left( \frac{A_g}{A_o} \right)^2 \quad (12)$$

$$I_{ij} \bar{u}_i = \frac{\rho}{L} \frac{k}{2} \left( \frac{A_g}{A_o} \right)^2 \bar{u}_i \quad (13)$$

The correlation 8 is used for the determination of the pressure loss coefficient  $k$ . This is available only for grills of regular geometric parameters only. The characterization of the upper grill of the TV-tuner is carried out numerically in a similar way as experimentally in a wind tunnel. Several computations are performed for different inlet velocities, providing the variation of the grill pressure drop with the mass flux. The inertial and viscous porous coefficients for the 2D and 3D resistance models are calculated using equations 10 and 9 respectively.

**Results of the detailed model** The static pressure recovery upstream the outlet grills occurs from 0.5 up to 1.5 orifice diameters as shown in annex, Table B.6. The distribution of the static pressure in these section planes can be seen in Fig. 20 for  $\omega = 5065$  rpm. The RMS of the static pressure drop and corresponding standard deviation are shown in Table 3. Relatively high values of the standard deviations are obtained for the grill of the upper wall as a result of the strong inhomogeneities of the static pressure. Moreover, as most of the fan flow between the lower and upper PCBs is directed to the left of the fan, the highest pressure drop is found through the sidewall grill one.

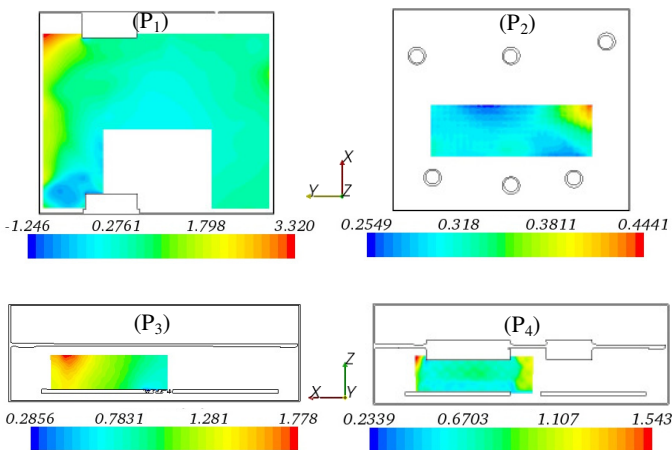


Figure 20. Static pressure distribution (Pa) in different section planes; results of the detailed model for  $\omega = 5065$  rpm.

	$\Delta p_{stat,RMS}$ (Pa)	$\sigma_p$ (Pa)
Upper wall	0.5053	0.5771
Lower wall	0.3061	0.02392
Sidewall 1	1.180	0.2614
Sidewall 2	0.7665	0.1997

Table 3. RMS of the static pressure drop through the outlet grills of the TV-tuner and corresponding standard deviation values.

**Results of the porous resistance models** The mass flow rate distribution predicted by the different numerical models is shown in Fig. 21. Compared to the results of the detailed computation, a similar distribution of mass flow rate obtained with the 2D porous model, while discrepancies in the mass flow rate up to 25% are found with the 3D porous resistance model.

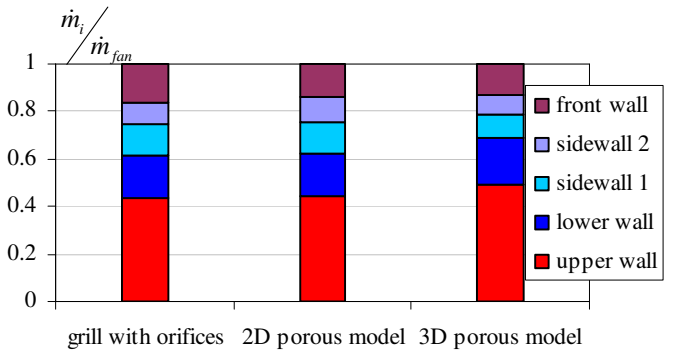


Figure 21. Mass flow rate distributions predicted by the different numerical models.

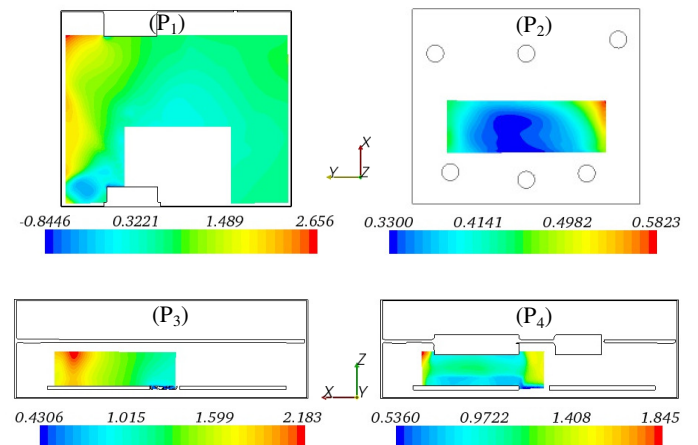
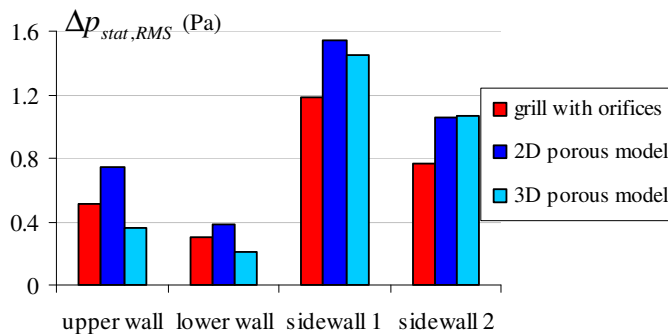


Figure 22. Static pressure distribution (Pa) in different section planes; results of the 2D porous model for  $\omega = 5065$  rpm.

The distribution of the static pressure computed by the 2D model can be seen in Fig. 22. The spatial distributions of the static pressure predicted by the porous resistance models are similar to the detailed computation solving the grill orifices. The comparison between the static pressure drop of the outlet grills provided by the detailed simulation and the porous resistance models is shown in Fig. 23. Overall, the static pressure drop predicted by the porous models is not consistent with the detailed computation. Strong discrepancies are found up to 46% for the upper grill.



**Figure 23. RMS of the static pressure drop through the outlets of the TV-tuner predicted by the different numerical models.**

## CONCLUSIONS

Numerical models for the prediction of the convective heat transfer mode in different types of flow encountered in electronic systems have been investigated in this paper. The range of validity of different approaches to solve the flow, which are required for the implementation in a co-simulation process, has been examined. For reasonable computing times in the development process, the flow has to be solved with steady-state computations. The range of validity of this approach has been investigated for the computation of buoyancy-driven flow, in particular for a range of Rayleigh number covering time-dependent convection. RANS turbulence models have been used. Flow structures consistent with the literature have been obtained with adapted initial conditions. However, the full convergence of the solution using the simple gradient diffusion hypothesis could not be reached. Moreover, the co-simulation processes assume flow computations with a flow initially isothermal at rest and suddenly subjected to a certain temperature distribution at the walls. The relevance of this type of initialization has been verified in particular in case of natural convection. The investigation showed that a correct structure of the flow could be reached with this kind of initialization only in cavities of similar aspect ratios in all directions. Furthermore, a steady-state method for fan flow simulation has been validated in comparison with the performance curve measured in the fan test-rig. With this method called MRF (Multiple Reference Frames), an accurate prediction of the fan pressure rise is achieved within 9.5% using a fine grid with minimum six cell layers in the fan near-wall

region. Finally, different numerical models have been investigated for flow computation through thin electronic grills in a TV-tuner, solving the flow through each grill orifice and using porous resistance models. Strong discrepancies of the RMS pressure drop through the grills have been obtained with the porous models. Therefore, the detailed computation solving the flow through each grill orifice has to be carried out.

## ACKNOWLEDGMENTS

This research was funded by Daimler AG, department EP/SAE. The authors would like to thank Prof. Thomas Breitling and Dr.-Ing. Raimund Siegert for supporting and approving the publication of the present work.

## REFERENCES

- [1] Michel, F., Desmet, B., 2010, "Transient numerical computation of the temperature of electronic devices in passenger cars", Paper No. 30122, 3<sup>rd</sup> Joint US-European Fluids Engineering Summer Meeting, ASME, Montréal.
- [2] Maveety, J.G., Leith, J.R., 1998, "Heat transfer in Rayleigh-Bénard convection with air in moderate size container", *Int. J. Heat Mass Transfer*, Vol. 41, Nos. 4-5, pp. 785-796.
- [3] Kirchartz, K.R., Oertel, H., 1988, "Three-dimensional thermal cellular convection in rectangular boxes", *J. Fluid Mech.*, Vol. 192, pp. 249-286.
- [4] Verzicco, R., Camussi, R., 2003, "Numerical experiments on strongly turbulent thermal convection in a slender cylindrical cell", *J. Fluid Mech.*, 477, pp. 19.
- [5] Pallares, J., Cuesta, I., Grau, F.X., 2002, "Laminar and turbulent Rayleigh-Bénard convection in a perfectly conducting cubical cavity", *Int. J. Heat Fluid Flow*, Vol. 23, pp.346-358.
- [6] Hsieh, K.J., Lien, F.S., 2004, "Numerical modeling of buoyancy-driven turbulent flows in enclosures", *Int. J. Heat Fluid Flow*, Vol. 25, pp. 659-670.
- [7] Chandra, L., Grötzbach, G., 2007, "Analysis and modeling of the turbulent diffusion of turbulent kinetic energy in natural convection", In: *Flow, turbulence and convection* 79, pp. 133-154.
- [8] Maughan, J.R., Incropera, F.P., 1987, "Experiments on mixed convection heat transfer for airflow in a horizontal and inclined channel", *Int. J. Heat Mass Transfer*, Vol. 30, No. 7, pp. 1307-1318.
- [9] Roeller, P.T., Stevens, J., Webb, B.W., 1991, "Heat transfer and turbulent flow characteristics of isolated protrusions in channels", *J. Heat Transfer*, Vol. 113, pp. 597-603.

[10]CD-Adapco Group, Methodology and User Guide, Computational Dynamics STAR-CD, Version 3.20, 2004, London.

[11]Jäger, W., 1982, „Oszillatorische und turbulente Konvektion“, Dissertation, University Karlsruhe, Germany.

[12]Leong, W.H., Hollands, K.G.T., Brunger, A.P., 1999, “Experimental Nusselt numbers for a cubical-cavity benchmark problem in natural convection”, Int. J. Heat Mass Transfer, Vol. 42, pp. 1979-1989.

[13]Belmonte, A., Tilgner, A., Libchaber, A., 1994, “Temperature and velocity boundary layers in turbulent convection”, Phys Review E, Vol. 50, Nr. 1, pp. 269-279.

[14]Hanjalic, K., Vasic, S., 1993, “Computation of turbulent natural convection in rectangular enclosures with an algebraic flux model”, Int. J. Heat Mass Transfer, Vol. 36, No. 14, pp. 3603-3624.

[15]Mc Allister, R.A., Ginnis, M.C., 1958, “Perforated-plate performance”, Chem. Eng. Sci., Vol.9, p.25.

[16]Mühle, J., 1972, „Berechnung des trockenen Druckverlustes von Lochböden“, Chemie-Ing.-Techn., Vol. 44, pp.72-79.

[17]Müller, M., Huth, M., Kleinhempel, S., 2006, „Messung des Druckabfalls an Lochblechen und Vergleich mit Literaturangaben“, DHBW Stuttgart.

## ANNEX A

### FLOW CHARACTERISTICS IN THE CAVITIES OF THE BACK BATTERY AND SOUND AMPLIFIER FOR STANDARD USE CASES

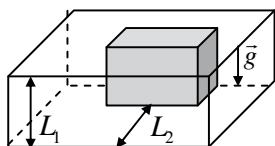


Figure A.1. Characteristic dimensions for the back battery.

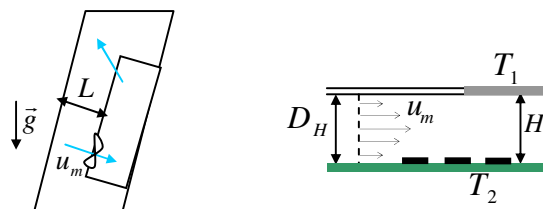


Figure A.3. Characteristic dimensions for the sound amplifier at the cavity level (left) or device level (right).

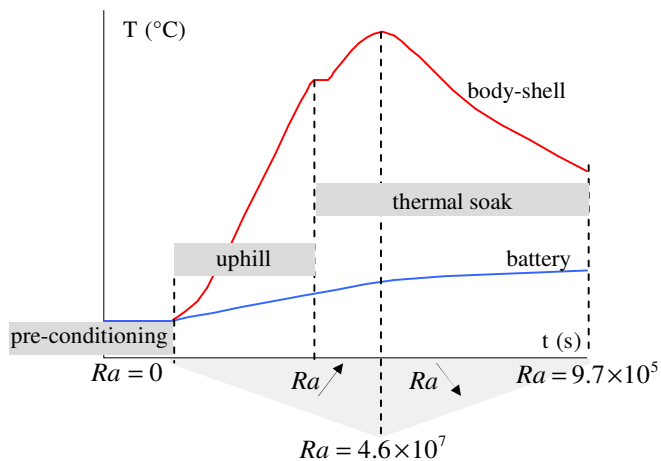


Figure A.2. Evolution of the Rayleigh number with time in the cavity of the battery during driving and soak phases.

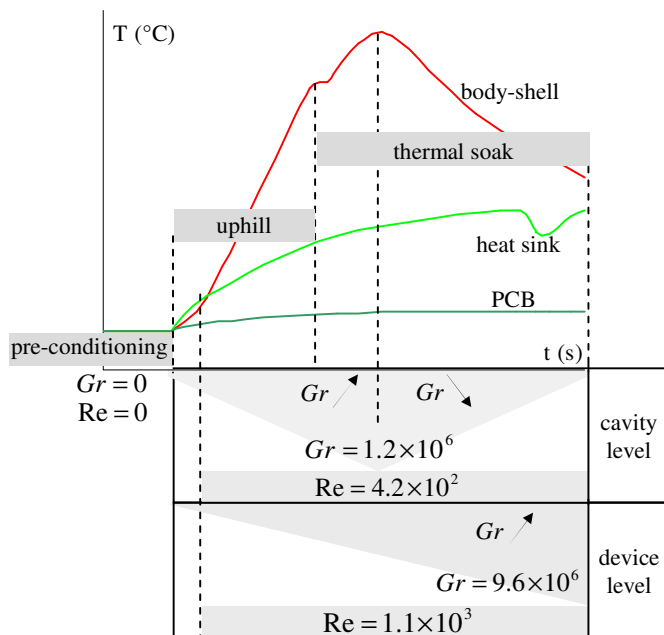


Figure A.4. Evolution of Rayleigh and Grashof numbers with time in the cavity of the amplifier during driving and soak phases.

## ANNEX B

### NUMERICAL MODELS FOR BUOYANCY-DRIVEN FLOWS, FAN FLOW SIMULATION AND FOR FLOW COMPUTATION THROUGH THIN ELECTRONIC GRILLS

Grid	Number of nodes $N_x \times N_y \times N_z = N^3$	Boundary layer	
		Number of layers	Range of $y^+$ values
BL9	72×72×72	9	[0; 2.4]
BL10	79×79×79	10	[0; 1.3]
BL12	85×85×85	12	[0; 1.2]
BL15	94×94×94	15	[0; 1.2]
BL20	109×109×109	20	[0; 0.8]

**Table B.1.** Grids generated for the investigation of mesh independency for buoyancy-driven flow in the cubical cavity.

Grid	Number of cells		Fan near-wall region, $y \leq 2 \times 10^{-4} m$	
	Fan	Elsewhere	Nb. of layers	Range of $y^+$ values
T2	$2.13 \times 10^6$	$3.84 \times 10^6$	2	[0; 23]
NW3	$5.44 \times 10^5$	$1.81 \times 10^6$	3	[0; 13]
NW6	$1.33 \times 10^6$	$1.81 \times 10^6$	6	[0; 12]
NW9	$1.87 \times 10^6$	$1.81 \times 10^6$	9	[0; 10]

**Table B.2.** Grid refinement for the MRF computations; fan of the sound amplifier in the test-rig.

	Upper wall	Lower wall	Sidewalls
Grill area $A_g$ (m <sup>2</sup> )	$1.80 \times 10^{-2}$	$5.21 \times 10^{-3}$	$1.20 \times 10^{-3}$
Total orifice area $A_o$ (m <sup>2</sup> )	$2.30 \times 10^{-3}$	$9.82 \times 10^{-4}$	$3.04 \times 10^{-4}$
Orifice diameter $d_o$ (m)	$4.00 \times 10^{-3}$	$2.50 \times 10^{-3}$	$3.00 \times 10^{-3}$
Orifice angular offset	45°	90°	45°
Orifice centre distance $p_o$ (m)	$9.00 \times 10^{-2}$	$5.00 \times 10^{-3}$	$5.00 \times 10^{-3}$
Grill plate thickness L (m)	$5.00 \times 10^{-4}$	$5.00 \times 10^{-4}$	$5.00 \times 10^{-4}$
Free area ratio $A_o / A_g$ (%)	8.25	18.8	25.3

**Table B.3.** Geometric parameters of the outlet grills of the TV-tuner.

	Perforated plate
Grill area $A_g$ (m <sup>2</sup> )	$4.34 \times 10^{-2}$
Total orifice area $A_o$ (m <sup>2</sup> )	$4.47 \times 10^{-3}$
Orifice diameter $d_o$ (m)	$8.00 \times 10^{-3}$
Orifice angular offset	45°
Orifice centre distance $p_o$ (m)	$2.14 \times 10^{-2}$
Grill plate thickness L (m)	$2.00 \times 10^{-3}$
Free area ratio $A_o / A_g$ (%)	10.3

**Table B.4.** Geometrical parameters of the perforated plate computed in the test-rig model.

Grid	Number of cells		Plate near-wall region, $y \leq 1 \times 10^{-3} m$	
	Plate	Elsewhere	Nb. of layers	Range of $y^+$ values
NW2	$1.85 \times 10^5$	$9.60 \times 10^5$	2	[0; 48]
NW3	$1.73 \times 10^6$	$9.60 \times 10^5$	3	[0; 20]
NW5	$3.78 \times 10^6$	$9.60 \times 10^5$	5	[0; 18]

**Table B.5.** Grid refinement for the computation of the flow through perforated plate in the test-rig model.

Outlet grill	Section plane	Normal distance to the grill inner wall	
		[m]	Nb. of orifice diameters
Upper wall	$P_1(x; y)$	$6 \times 10^{-3}$	1.5
Lower wall	$P_2(x; y)$	$2.5 \times 10^{-3}$	1
Sidewall 1	$P_3(x; z)$	$3 \times 10^{-3}$	1
Sidewall 2	$P_4(x; z)$	$1.5 \times 10^{-3}$	0.5

**Table B.6.** Section plane for the evaluation of the static pressure drop of the outlet grills.